J Adv Ceram

Research Article

Synergistic shallow impurity levels and multiscale defect engineering in GeTe-based thermoelectrics

Zhongwei Zhang[1,2], Fengting Mao[2], Min Yao[2], Shiyuan Zhao[2], Sijing Zhu[2], Zhengniu Pan[2], Jun-Liang Chen[3], Zhixiang Zhang[3], Qi Zhou[2], Wentao Zhang[4], Jianmin Chen[4], Jie Gao[3,✉], Lei Miao[2,✉]

Cite this article: Zhang Z, Mao F, Yao M, et al. *J Adv Ceram* 2026, **15**(3): 9221258. https://doi.org/10.26599/JAC.2026.9221258

ABSTRACT: By the coordinated implementation of shallow impurity level and multiscale defect engineering, this study achieves the simultaneous optimization of electrical transport and thermal conduction in GeTe-based thermoelectric (TE) materials. This synergistic mechanism originates from the unique electronic configuration of Ni, whose d–sp orbital hybridization introduces shallow impurity levels that promote valence band convergence, thereby enhancing the effective mass of carriers and the Seebeck coefficient. Concurrently, *in situ* reactions between Ni and Ge form NiGe nanophases (10–30 nm), constructing multiscale defect structures that enable full-spectrum phonon scattering and suppress the lattice thermal conductivity of the $Ge_{0.885}Sb_{0.1}Ni_{0.015}Te$ sample to ~0.8 $W{\cdot}m^{-1}{\cdot}K^{-1}$ at 323 K. Leveraging this cooperative optimization, $Ge_{0.885}Sb_{0.1}Ni_{0.015}Te$ attains a peak dimensionless figure of merit (ZT) value of 2.15 at 773 K and an average ZT_{avg} of ~1.45 (323–773 K). A fabricated single-leg device achieves a conversion efficiency of ~10% under ΔT = 420 K, ranking among the top performances in the field. This work establishes a solid foundation for enhancing the performance and expanding the applications of GeTe-based TE materials.

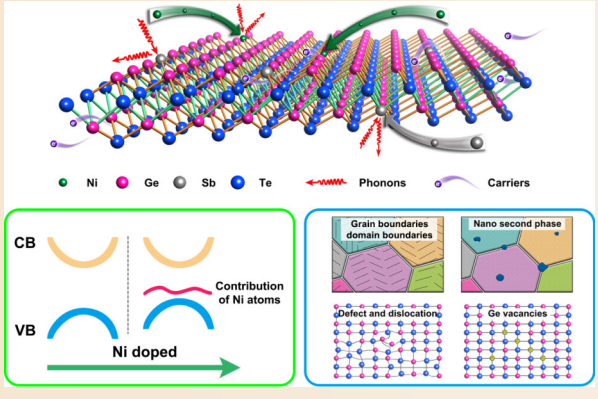

KEYWORDS: multiscale defect engineering; shallow impurity level engineering; valence band convergence; GeTe-based materials

1 Introduction

Thermoelectric (TE) materials, which directly transform industrial waste heat into electricity through the Seebeck effect, offer promising pathways for energy conversion and serve as cornerstone technologies in carbon neutrality strategies [1–3]. The thermoelectric conversion efficiency of a material is quantified by the dimensionless figure of merit $ZT = S^2\sigma T/\kappa$, where S, σ, T, and κ, denote the Seebeck coefficient, electrical conductivity, absolute temperature, and total thermal conductivity, respectively ($\kappa = \kappa_e + \kappa_l$, κ_e and κ_l denote the electronic and lattice thermal conductivities, respectively) [4–6]. Performance enhancements in common TE materials such as Bi_2Te_3, PbTe, and SnSe typically involve strategies such as band convergence or nanostructuring [7–10]. However, these materials still encounter intrinsic limitations, particularly regarding ecotoxic constituents (e.g., Pb/Cd) and restricted temperature operating windows. In contrast, GeTe demonstrates exceptional promise due to its innate ability to concurrently engineer band structures and evolve hierarchical defect systems, which enables simultaneous optimization of charge transport and suppression of phonon propagation [2,11]. This intrinsic mechanism contributes to achieving extraordinary TE performance.

GeTe emerges as a viable lead-free alternative among chalcogenide TEs with significant potential. When cooling below 700 K, the Ge atom off-centering displacement along the [111] crystallographic direction triggers a reversible phase transition from the cubic phase ($Fm\bar{3}m$) to rhombohedral symmetry ($R3m$) [12–14]. This structural evolution fundamentally establishes multiple valence bands with minimal energy offsets in its electronic structure. Moreover, intrinsic Ge vacancies exhibit exceptionally low formation energy, inducing carrier concentrations approaching ~10^{21} cm^{-3}, which substantially deviates from the TE optimum range [15]. Leveraging these dual attributes of tunable band structures and carrier concentration, researchers employ comprehensive strategies, including carrier engineering, charge transfer engineering, band optimization, and defect architecture design, to decouple adversarial TE parameter

[1] School of Chemistry and Chemical Engineering, Guangxi University, Nanning 530004, China. [2] School of Physical Science and Technology, Guangxi University, Nanning 530004, China. [3] Guangxi Key Laboratory of Information Materials, Guangxi Collaborative Innovation Center of Structure and Property for New Energy Materials, Guilin University of Electronic Technology, Guilin 541004, China. [4] Henan Hongchang Electronics Co., Ltd., Xuchang 461500, China.

✉ Corresponding authors. E-mail: J. Gao, gaojie@guet.edu.cn; L. Miao, miaolei@gxu.edu.cn

Received: December 26, 2025; Revised: January 31, 2026; Accepted: February 4, 2026

relationships. Whether employing donor species such as Bi^{3+} or Sb^{3+} to supply electrons, Pb^{2+} substitution for passivating Ge vacancy sites, or Ge self-compensation, these mechanisms optimized carrier concentrations within an ideal range without compromising high carrier mobility [16–18]. Separately, charge transfer engineering taps into the inherent resonant bonds of GeTe, concentrating on localized charge displacement from elemental doping and micronanostructures to enable advanced carrier transportation synergized with extensive phonon suppression across the material [11].

Band engineering serves as a fundamental TE optimization strategy, especially for GeTe-based systems. In GeTe, the highest occupied molecular orbital (HOMO) and lowest unoccupied molecular orbital (LUMO) are predominantly governed by Te $5p^4$ and Ge $4p^2$ orbitals, while Ge $4s^2$ and Te $5s^2$ primarily contribute to lower energy valence bands. Hybridization between the Ge 4s lone pair and Te 5p orbitals results in a pronounced multivalley band structure [19,20]. During the phase transition from $R3m$ to $Fm\bar{3}m$, the bandgap evolves from indirect to direct character. Building on this tunable electronic framework, researchers harness element doping to modulate orbital hybridization, achieving band convergence, bandgap tuning, and the introduction of resonant levels and shallow impurity levels [21–23]. For example, doping with transition elements such as Mn or Co induces strong p–d orbital interactions, effectively reducing energy separation between light and heavy valence bands to facilitate band convergence [20,24]. Moreover, dopants lacking s^2 lone pairs (e.g., Zn or Cd) attenuate the Ge $4s^2$ contribution to the HOMO orbital, suppressing lattice distortion to stabilize the cubic phase and promote valence band convergence [25,26]. Dopants such as indium (In) or Ga modify the band structure by adjusting the local density of states near the Fermi level, creating a pseudogap structure at the valence band edge that selectively transports high-energy carriers while blocking low-energy carriers [27–31]. Meanwhile, interstitial Cu^+ ions optimize carrier dynamics through shallow impurity bands, beneficially regulating the effective mass and mobility correlation [32,33]. Together, these synergistic band-structure modifications establish a robust foundation for enhancing thermoelectric performance.

Defect engineering represents the central strategy for GeTe-based TE enhancement, relying on multiscale defect coordination to uncouple carrier–phonon transport parameters [34–37]. Utilizing intrinsic high-density Ge vacancies, high-temperature annealing induces ordered dislocation loops and van der Waals gap formations that efficiently scatter mid-frequency phonons while preserving carrier transport integrity, achieving an ultralow κ_l of ~0.48 $W \cdot m^{-1} \cdot K^{-1}$ [16,38]. Heteroatomic doping further introduces multidimensional defects, enabling full-spectrum phonon scattering. Synergistic Y/Sb/Ag codoping suppresses the lone pair electrons of Ge^{2+} ions, suppressing lattice distortion and forming atomically ordered zigzag planar defects [11]. A dilute doping strategy incorporating 4% $CuSbPbTe_3$ constructs multidimensional defect networks in GeTe, comprising zero-dimensional interstitial Cu atoms, two-dimensional vacancy planes, and three-dimensional nanoscale amorphous GeO_2 [32]. Similarly, Fe doping forms nanocomposites with Ge vacancy-rich shells surrounding Fe_2Ge cores that substantially attenuate phonon propagation [39]. Collectively, future efforts will refine multiscale defects to sustain full-spectrum phonon scattering while preserving superior charge transport efficiency.

While GeTe is a promising TE material, its performance is often limited by the interdependent trade-off between electronic and thermal transport properties, alongside challenges in achieving optimal carrier concentration and effective phonon scattering. To address these issues, this work integrates shallow impurity level engineering with multiscale defect engineering to synergistically optimize carrier transport and suppress phonon propagation, enhancing the integrated TE properties of GeTe-based materials (Fig. 1(a)). Specifically, Sb doping is used to tune the carrier concentration of GeTe toward the ideal range, while Ni doping induces d–sp orbital hybridization (Fig. 1(b)). This promotes valence band convergence and introduces shallow impurity states near the band edge, which together increase the carrier effective mass and yield a high Seebeck coefficient of ~232 $\mu V \cdot K^{-1}$ at 773 K. Elemental doping simultaneously reduces grain dimensions and generates dislocations with Ge vacancies, with Ni concurrently reacting *in situ* to form NiGe secondary phases (Fig. 1(c)). This establishes multiscale defect networks that scatter phonons across all dimensions and reduce κ_l in $Ge_{0.885}Sb_{0.1}Ni_{0.015}Te$ to ~0.8 $W \cdot m^{-1} \cdot K^{-1}$. The cooperative optimization enhances the weighted mobility to lattice thermal conductivity ratio (μ_w/κ_l), especially in $Ge_{0.885}Sb_{0.1}Ni_{0.015}Te$ (Fig. 1(d)). Consequently, $Ge_{0.885}Sb_{0.1}Ni_{0.015}Te$ reaches a peak ZT of ~2.15 at 773 K and an average ZT_{avg} of ~1.45, which is at the forefront level (Fig. 1(e)) [11,27,37,40,41]. From a practical standpoint, the partial substitution of expensive Ge with more abundant and lower cost Ni and Sb also addresses the critical cost concerns for potential commercialization. Employing a precision interfacial design, we fabricated single-leg TE devices with Fe electrodes and SnTe diffusion barriers. This single-leg TE device achieves a peak energy conversion efficiency (η_{max}) of ~10.1% when operating under a ΔT of ~420 K, ranking among the top performances in the field (Fig. 1(f)) [11,16,42,43]. This device leads existing counterparts significantly, establishing a critical foundation for practical GeTe-based TE modules.

2 Materials and methods

2.1 Synthesis of samples

The sample preparation process commenced within an argon-filled glove box where high-purity Ge (99.99%, ZhongNuo Advanced Material Technology), Sb (99.99%, Aladdin), Ni (99.99%, Aladdin), and Te (99.99%, ZhongNuo Advanced Material Technology) were precisely weighed according to stoichiometric ratios $Ge_{0.9-x}Sb_{0.1}Ni_xTe$ (x = 0.005–0.02) before transferring to a quartz tube. The mixtures were sealed in quartz tubes, purged thrice with high-purity nitrogen, and vacuum-sealed below 10 Pa. Tubes were heated to 1273 K over 12 h in a muffle furnace, held for 12 h, and then slowly cooled to room temperature over 12 h. Ingots were ground in an agate mortar for 20 min, loaded into graphite dies, and cold-pressed at 15 MPa for 1 min to evacuate gases. Spark plasma sintering was applied at 50 MPa while ramping to 823 K in 15 min with a 30-min dwell period. Pressure was released at 673 K during natural cooling. The resulting bulks were polished, sectioned into plates/bars via diamond wire sawing, and subjected to thermoelectrical property assessment and microstructural characterization.

2.2 Measurement of properties

The 3 mm × 3 mm × 12 mm metal bars were characterized in a helium-purged ZEM-3 system (ADVANCE RIKO, Japan) to simultaneously determine the Seebeck coefficient S and electrical conductivity σ with a combined uncertainty of ±7%. Thermal diffusivity D was measured on ϕ12.60 mm × 1 mm discs using an LFA 467 HT laser analyzer (NETZSCH, Germany) within ±6% error, enabling calculation of total thermal conductivity κ via $\kappa = Dc_p\rho$. Here, the specific heat c_p was derived from the Dulong–Petit

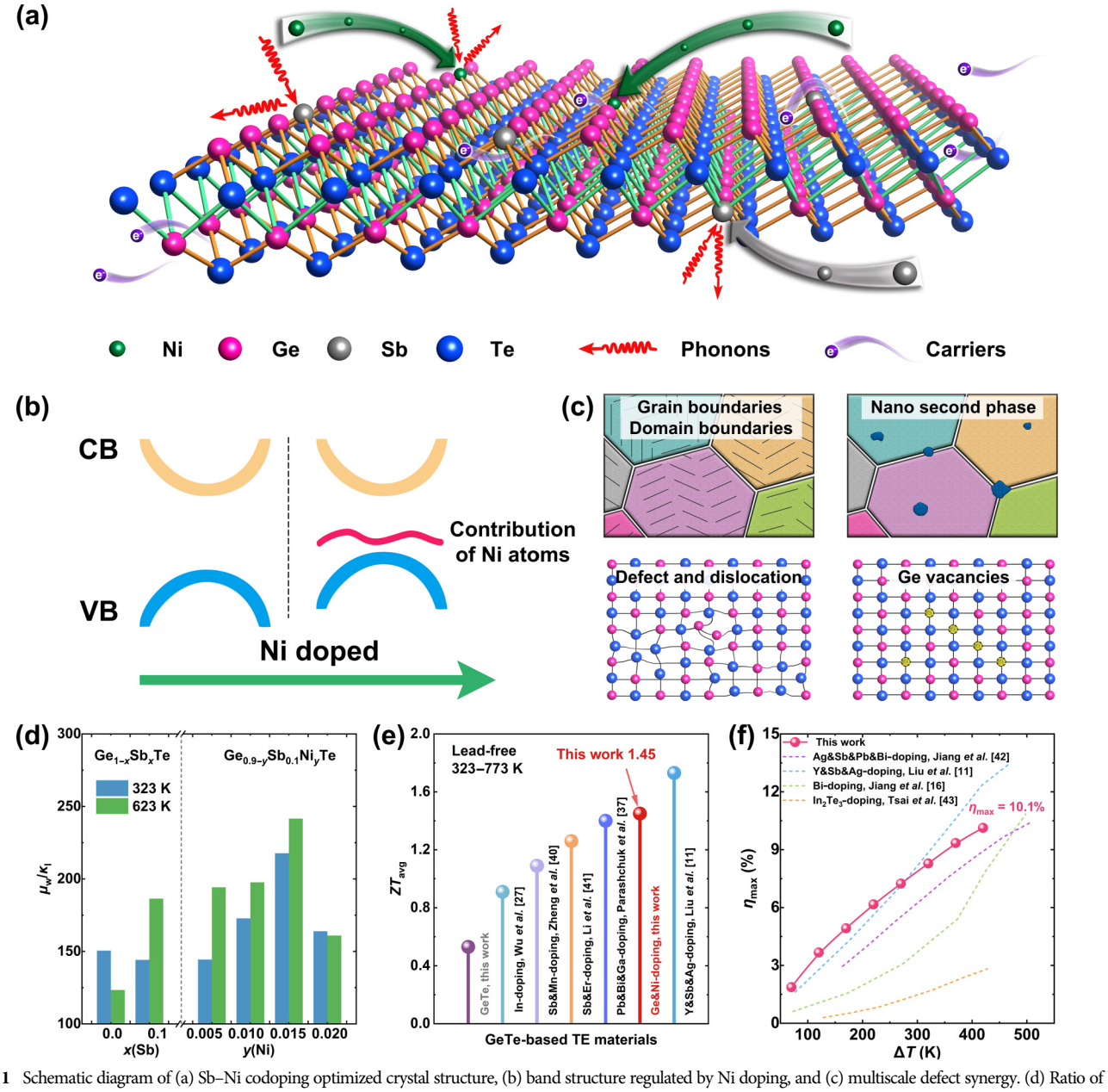

Fig. 1 Schematic diagram of (a) Sb–Ni codoping optimized crystal structure, (b) band structure regulated by Ni doping, and (c) multiscale defect synergy. (d) Ratio of weighted mobility to lattice thermal conductivity of $Ge_{0.89-x}Sb_{0.1}Ni_xTe$ (x = 0.005–0.02). Comparison with literature on (e) ZT_{avg} over 323–773 K [11,27,37,40,41] and (f) peak conversion efficiency (η_{max}) of single-leg devices [11,16,42,43].

limit, while the mass density ρ was obtained by Archimedes' method as documented in Table S1 in the Electronic Supplementary Material (ESM). Hall coefficient R_H measurements on 10 mm × 10 mm × 0.9 mm samples employed a LakeShore 8404 magnetometer system (USA), from which carrier concentration n_H and mobility μ_H were extracted using $n_H = 1/(eR_H)$ and $\mu_H = \sigma R_H$, respectively, with e corresponding to the elementary charge.

2.3 Material characterization

Powder X-ray diffraction (PXRD) patterns were acquired using Cu Kα radiation (λ = 0.154 nm) on a Bruker D8 Advance diffractometer with a scan range of 10°–100° (step size 0.01°). Microstructural and elemental distribution analyses were conducted via a transmission electron microscope (TEM; Talos F200X, USA) equipped with an integrated Super-X energy dispersive spectrometer (EDS) system complemented by quantitative microanalysis using an electron probe microanalyzer (JXA-8230, Japan).

2.4 First-principles calculations

First-principles computations were performed via the Vienna *Ab initio* Simulation Package (VASP). The Perdew–Burke–Ernzerhof (PBE) generalized gradient approximation (GGA) functional described exchange–correlation interactions and projector augmented wave method was used for electron–ion interactions. A 3×3×3 GeTe supercell was constructed with Sb/Ni atoms substitutionally replacing Ge sites. Post full structural relaxation, electronic band structures, projected density of states, and Bader charges were analyzed. Notably, spin-orbit coupling was included in band calculations but omitted during structural optimization.

2.5 Single-leg device fabrication

Single-leg thermoelectric devices with Fe electrodes were

consolidated by spark plasma sintering. Fe-, SnTe-, and GeTe-based powders were sequentially loaded into a graphite die. The temperature was ramped to 853 K at 10 K·min^{-1} and held for 30 min under axial pressure. Pressure was released during slow cooling to 673 K. A SnTe interlayer was integrated between the GeTe matrix and Fe electrodes. The contact resistivity was measured by a four-point probe method with a movable tip. The energy conversion efficiency η was characterized using $\eta = P_{out}/(Q_c + P_{out} + Q_r)$, where P_{out} denotes the output power, Q_c represents the cold-end heat flux quantified through water temperature calibration, and Q_r corresponds to radiative dissipation estimated from device dimensions.

3 Results and discussion

As shown in Fig. 2, the lattice structures of samples GeTe, $Ge_{0.9}Sb_{0.1}Te$, and $Ge_{0.9-x}Sb_{0.1}Ni_xTe$ (x = 0.005–0.02) are characterized using XRD patterns. Codoping of Sb and Ni profoundly modifies the GeTe crystal structure (Fig. 2(a)). Relative to standard rhombohedral GeTe diffraction (PDF#00-047-1079), Sb doping induces a leftward shift of the dominant peak (202) with concurrent convergence between peaks (024) and (220) [44]. This phenomenon originates from Sb (1.45 Å) substitution at Ge (1.24 Å) sites featuring a larger atomic radius [45]. However, weak diffraction shifts are caused by limited Ni doping. Pronounced Ge enrichment phases occur in pristine GeTe and Sb-doped samples due to low vacancy formation energy, while Ni doping efficiently suppresses such precipitation through *in situ* formation of NiGe secondary nanophases. The XRD refinement quantitatively reveals structural evolution (Fig. S1 in the ESM). Sb doping with a larger atomic radius expands the lattice parameters $a = b$ to ~4.22 Å while contracting c to 10.58 Å (Fig. 2(b)). Subsequently, the slightly smaller atomic radius of Ni (1.21 Å) compared with Ge

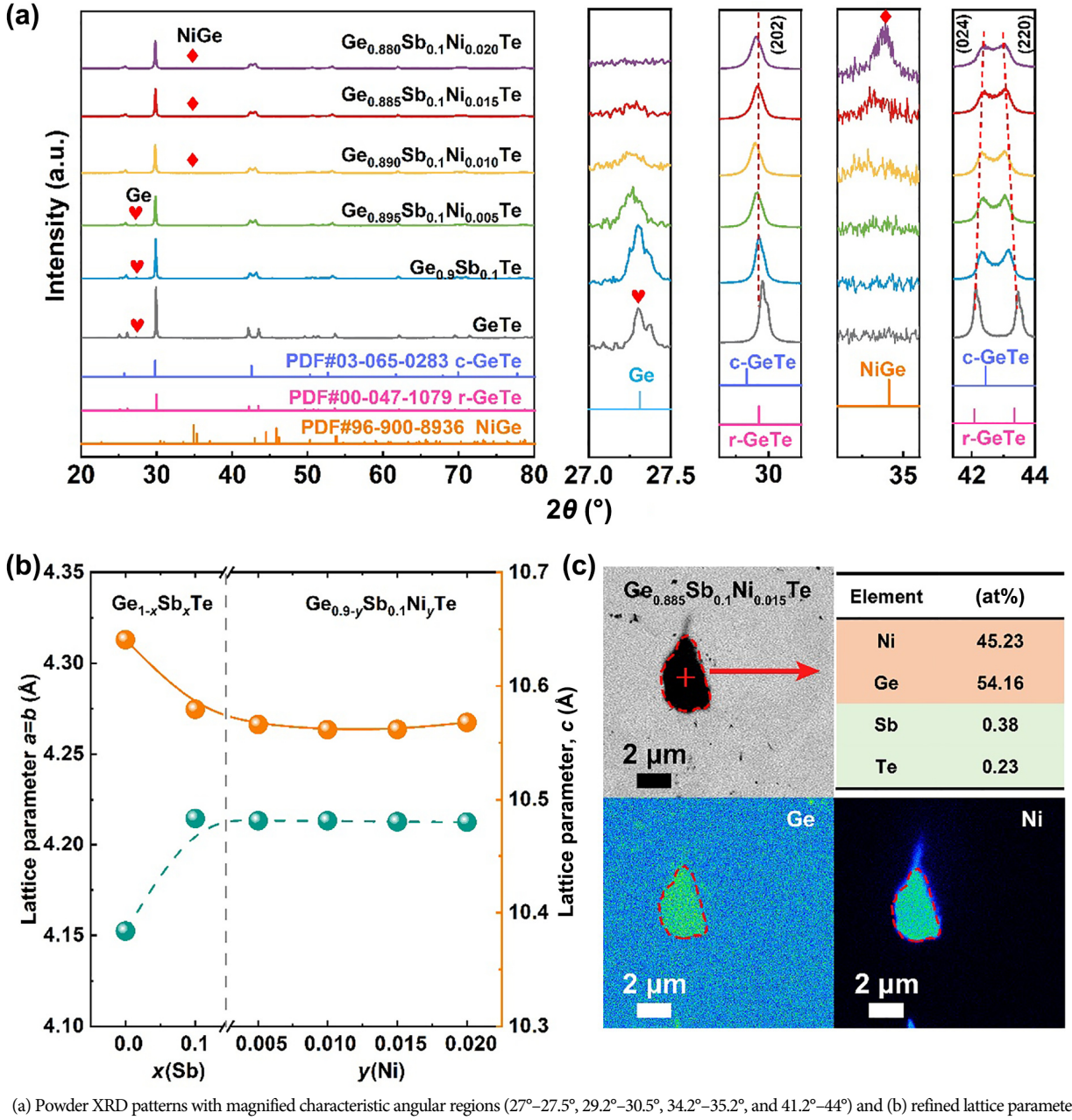

Fig. 2 (a) Powder XRD patterns with magnified characteristic angular regions (27°–27.5°, 29.2°–30.5°, 34.2°–35.2°, and 41.2°–44°) and (b) refined lattice parameters $a = b$ and c of $Ge_{0.89-x}Sb_{0.1}Ni_xTe$ (x = 0.005–0.02). Heart-shaped symbol represents Ge-enriched phase, and diamond symbol represents NiGe orientation. (c) EPMA elemental mapping and point quantification of $Ge_{0.885}Sb_{0.1}Ni_{0.015}Te$.

results in limited influence on the shorter-bonded *a* and *b* directions via bond relaxation while inducing a slight contraction along the longer-bonded *c* axis, leading to an overall reduction in lattice volume (Fig. S2 in the ESM) [46]. This *c*-axis-dominated compression confirms partial Ni occupation at Ge sites. This substitutional doping is corroborated by quantitative microscale characterization. Point scan analyses show that most Ni is homogeneously dispersed within the matrix, with an average stoichiometry close to the nominal value of ~0.0144, slightly lower than the target of 0.015 (Figs. S3 and S4 in the ESM). The minor shortfall is mainly due to some Ni forming a NiGe secondary phase. Electron probe microanalyzer (EPMA) mapping reveals NiGe nanophase formation, and point scans verify a local composition consistent with NiGe (Fig. 2(c)). The XRD refinement data in Table S2 in the ESM further establish a positive correlation between the NiGe concentration and Ni doping level.

Figure 3 presents the temperature-dependent electrical properties of samples GeTe, $Ge_{0.9}Sb_{0.1}Te$, and $Ge_{0.9-x}Sb_{0.1}Ni_xTe$ (x = 0.005–0.02). The positive Seebeck coefficients across all samples confirm characteristic p-type degenerate semiconductor behavior [47,48]. Sb donor doping reduces the carrier concentration (n_H) by nearly one order of magnitude, directly decreasing σ from 7×10^5 to ~10^5 S·m^{-1} (Fig. 3(a)). Further Ni doping mildly distorts the lattice structure, lowering σ to 9×10^4 S·m^{-1}. The change in carrier scattering behaviors is revealed through conductivity slope variations [49,50]. This transition arises from the evolution of scattering mechanisms, wherein acoustic phonon scattering dominates in pristine GeTe systems and generates $T^{-3/2}$ weighted mobility scaling, while alloy scattering governs Sb/Ni codoped counterparts with mobility shifting to $T^{-1/2}$ dependence, as demonstrated in Fig. 3(b) [51,52].

Crucially, doping simultaneously enhances *S*. Specifically, the Sb dopant elevates *S* from 45.8 to 111.2 μV·K^{-1} at 323 K, while Ni doping further increases *S* to 132.9 μV·K^{-1} (Fig. 3(c)). This additional improvement in *S* directly enhances the power factor (PF) across all temperatures. The result is a power factor of 40.7 μW·cm^{-1}·K^{-2} at 600 K, representing an ~31% increase over the base value of 34.2 μW·cm^{-1}·K^{-2}, achieved via the synergistic effect of distinct dopant mechanisms (Fig. 3(d)). Sb doping markedly reduces carrier concentration and mobility, as tabulated in Fig. 3(e) and Table S3 in the ESM, whereas Ni doping marginally increases concentration yet persistently suppresses mobility. The effective carrier mass increases from $1.35m_0$ to $1.96m_0$ (where m_0 is the free electron rest mass) with Sb/Ni codoping, as determined from *S*–*n* diagram fitting. This trend agrees with earlier reports and highlights the distinct contribution of Ni [11,16,27,53]. Similar behavior in In-doped systems corroborates that the gain in effective mass is the key mechanism behind the enhanced Seebeck coefficient [27,53].

To better understand how Ni functions in the GeTe system, we used first-principles calculations to assess its influence on the electronic structure. The first-principles calculations elucidate the electronic structures and density of states for rhombohedral $Ge_{27}Te_{27}$, $Ge_{26}Ni_1Te_{27}$, and $Ge_{25}Sb_1Ni_1Te_{27}$ (Fig. 4). As depicted in Fig. 4(a), the valence band maximum of GeTe primarily depends on Te 5p orbitals, while the conduction band is dominated by Ge 4p states, with the density of states confirming this distribution (Fig. 4(d)). The Ni doping generates a distinct shallow impurity level near the Fermi energy (Fig. 4(b)), with orbital-resolved analysis confirming predominant origination from Ni 3d orbitals (Fig. 4(e) and Fig. S5 in the ESM). This phenomenon arises from the unique electronic configuration of Ni (ground state [Ar] $3d^84s^2$) [54]. Upon substitutional doping at Ge sites, Ni loses its $4s^2$ electrons, adopting a stable Ni^{2+} configuration [Ar] $3d^8$, as

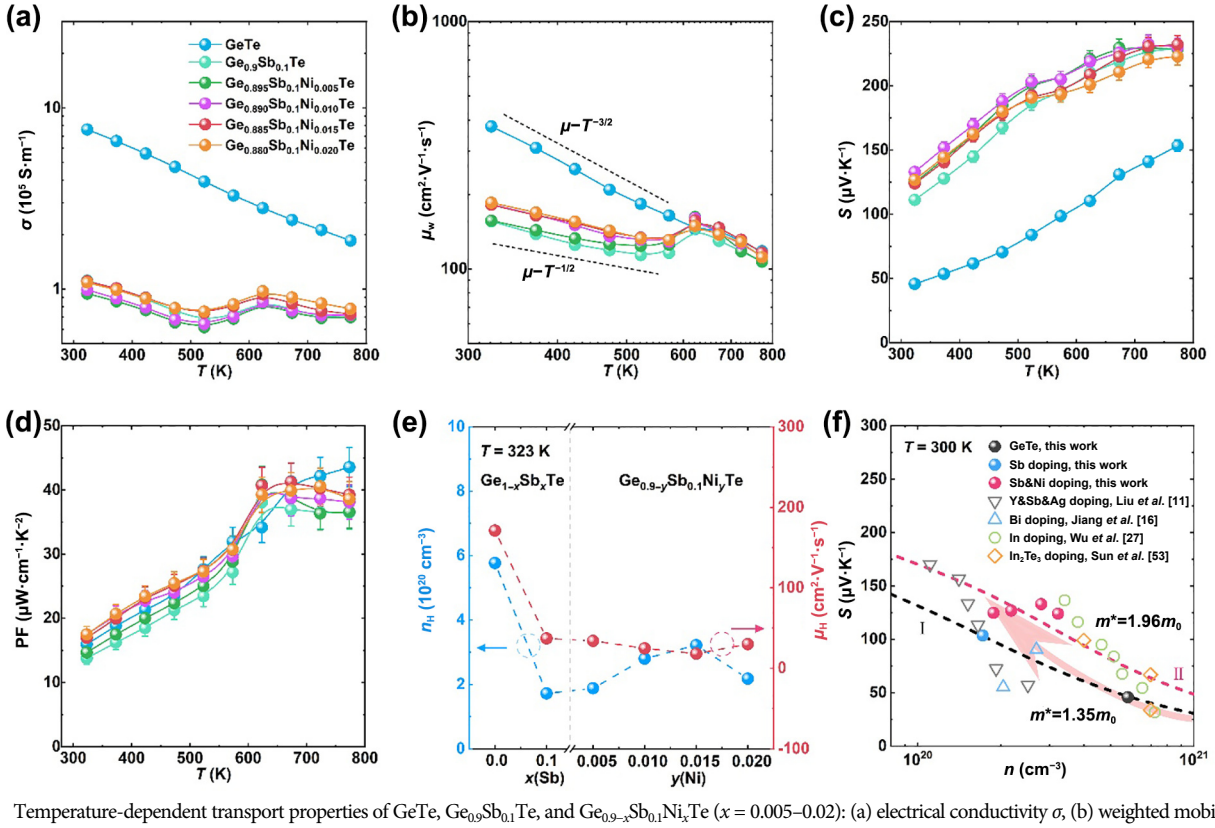

Fig. 3 Temperature-dependent transport properties of GeTe, $Ge_{0.9}Sb_{0.1}Te$, and $Ge_{0.9-x}Sb_{0.1}Ni_xTe$ (x = 0.005–0.02): (a) electrical conductivity σ, (b) weighted mobility μ_w, (c) Seebeck coefficient *S*, (d) power factor PF. (e) Carrier concentration n_H and mobility μ_H evolve with doping concentration. (f) Comparison of *S*–*n* relationship diagram of GeTe codoped with Sb and Ni with literature [11,16,27,53].

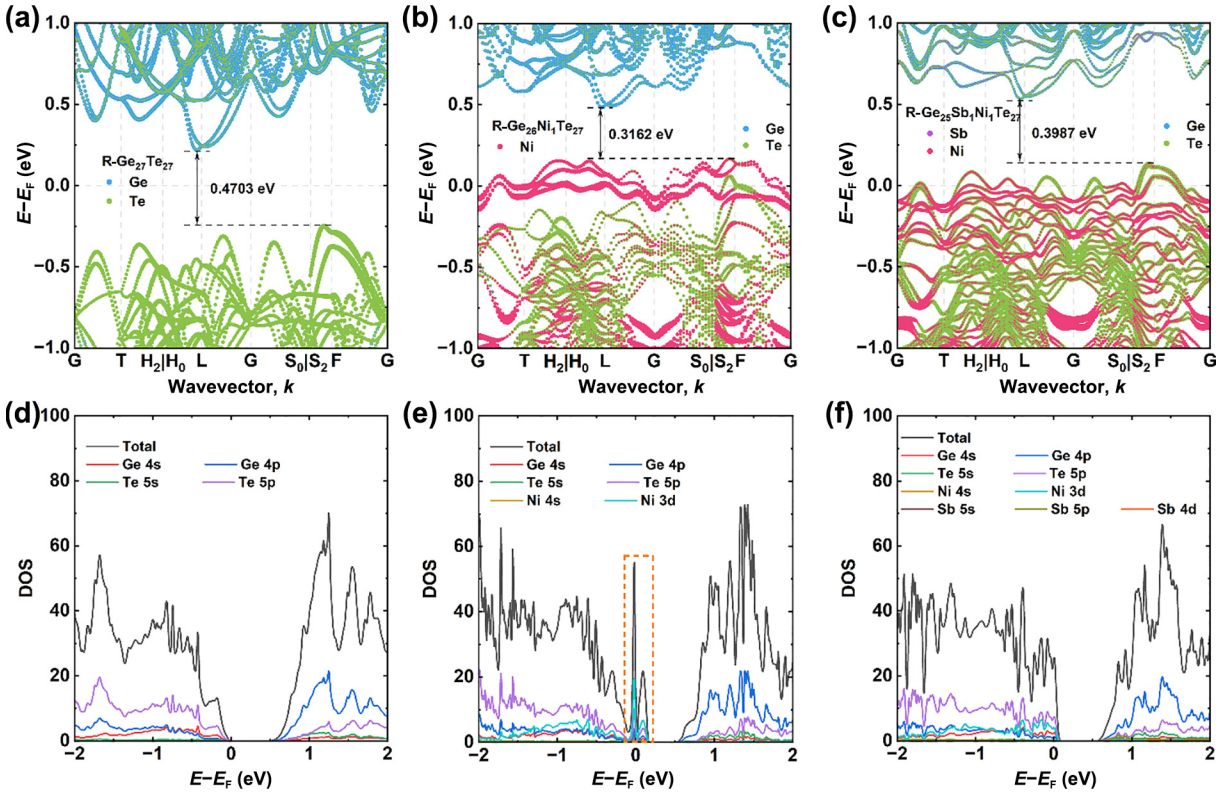

Fig. 4 (a–c) Band structures and (d–f) corresponding density of states plots for rhombohedral $Ge_{27}Te_{27}$, $Ge_{26}Ni_1Te_{27}$, and $Ge_{25}Sb_1Ni_1Te_{27}$ obtained from first-principles calculations. Here, the prefix "R-" denotes the rhombohedral phase.

confirmed by X-ray photoelectron spectra (XPS) (Fig. S6 in the ESM). Beyond the involvement of the 4s orbital, the Ni $3d^8$ configuration exhibits a clear arrangement of energy levels under the octahedral crystal field of GeTe, facilitating the formation of shallow impurity levels. Near the Fermi level, the Ni 3d orbitals hybridize with the Te 5p orbitals via sp–d hybridization. The weak magnetic moment of Ni may become active only in the rhombohedral phase, whereas it is quenched in the cubic phase due to strong sp–d orbital hybridization [55]. This differs from reported Cd ([Kr] $4d^{10}5s^2$) and Zn ([Ar] $3d^{10}4s^2$) doping cases where only s orbitals hybridize, as their filled d orbitals remain inactive [26,56]. Although Fe and Co have similar electronic configurations and may introduce impurity levels of a comparable nature, the metastable nature of their d orbitals results in a limited contribution to the overall thermoelectric performance (Fig. S7 in the ESM) [24,39]. Furthermore, in GeTe, Ge $4s^2$ orbitals contribute to deep valence bands but negligibly affect the valence band maximum, exacerbating energy offsets (ΔE) between multiple valence bands [57]. The Ni 3d orbitals partially suppress Ge $4s^2$ lone-pair character at the band edge, diminishing residual contributions and promoting valence band convergence (reduced ΔE), thereby enhancing thermoelectric transport (Fig. S8 in the ESM). Under Sb and Ni codoping (Figs. 4(c) and 4(f)), d–sp hybridization persists, while Sb synergistically facilitates band alignment, jointly optimizing the carrier effective mass and S.

Ni doping not only modulates the electronic structure but also induces complex ordered microstructures. The pristine GeTe exhibits a characteristic herringbone pattern of ferroelectric domains (Figs. 5(a) and 5(b)), where the alternating contrast signifies regions with opposing polarizations [58,59]. High-resolution imaging confirms the crystal structure, which aligns well with the XRD reference pattern (PDF#00-047-1079). With Ni doping, the low-magnification TEM image of $Ge_{0.885}Sb_{0.1}Ni_{0.015}Te$ reveals ferroelectric domains slightly distinct from those observed in pristine GeTe, showing more random distribution and size variations. This observation aligns with previously reported findings [38,42]. The introduction of Sb and Ni dopants into the GeTe lattice induces distinct structural modifications where the larger atomic radius of Sb drives lattice expansion, while Ni doping leads to c-axis contraction, collectively resulting in lattice distortion. These distortions generate randomly distributed strain fields within the material, thereby promoting spatial randomness in the distribution of domain walls and defects along with significant size variations.

Further TEM analysis reveals the presence of nanosecondary phases with dimensions ranging from 10 to 30 nm in $Ge_{0.885}Sb_{0.1}Ni_{0.015}Te$. The EDS analysis identifies these nanoprecipitates as NiGe compounds and Ge-enriched phases, consistent with the XRD results (Fig. S3 in the ESM). This phenomenon occurs because a small fraction of Ni dopants do not incorporate into the GeTe lattice but instead react *in situ* with Ge-rich regions, forming NiGe nanoparticles. These particles effectively impede phonon transport, thereby reducing the κ. In addition, pronounced lattice distortions induced by doping lead to the formation of dislocations along ferroelectric domain walls in $Ge_{0.885}Sb_{0.1}Ni_{0.015}Te$, as shown in Fig. 5(f). Concurrently, the extensive stress–strain fields created by doping serve as nucleation sites for defect formation [60,61]. Figures 5(g) and 5(h) exemplify such microstructural features, where the region marked "H" exhibits distinct lattice defects with geometric phase analysis confirming substantial strain fields localized around these defects. The high-resolution imaging further reveals both isolated and continuous Ge vacancies (planar defects), which are randomly distributed primarily within ferroelectric domains [62]. These vacancies provide additional phonon scattering sites (Fig. S9 in the ESM). This multiscale defect architecture, comprising nanoscale

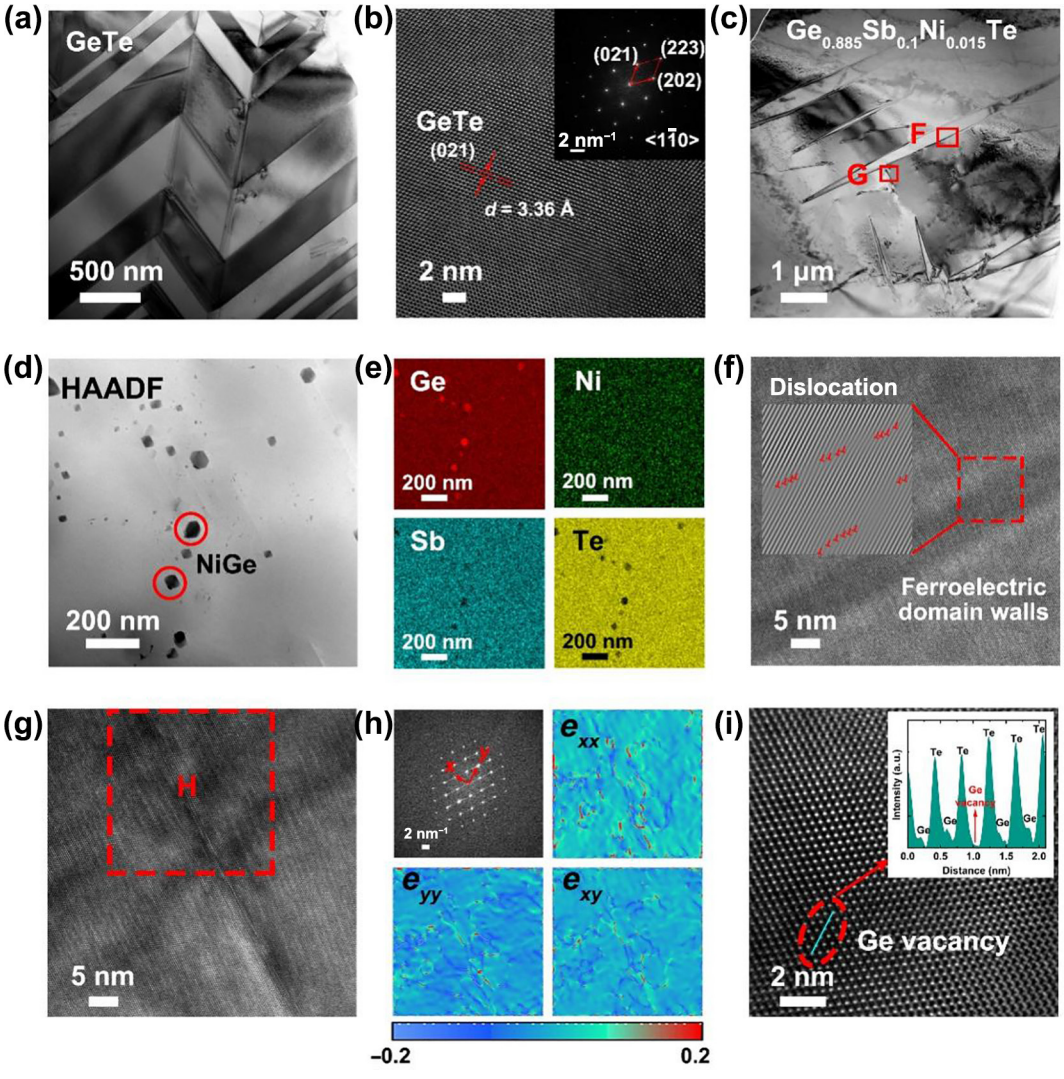

Fig. 5 (a, b) Low-magnification TEM and high-resolution TEM images of pristine GeTe with insets displaying Fourier transform (FFT) patterns. (c) Low-magnification TEM image, (d) nanostructured secondary phase morphology, and (e) corresponding elemental maps of $Ge_{0.885}Sb_{0.1}Ni_{0.015}Te$. (f) TEM image near ferroelectric domain (region F in (c)) in $Ge_{0.885}Sb_{0.1}Ni_{0.015}Te$ with inset showing inverse Fourier transform (IFFT) analysis of dislocations. (g) Magnified view of defect region G marked in (c) and (h) its geometric phase analysis of region H in (g). (i) Ge vacancies identified in $Ge_{0.885}Sb_{0.1}Ni_{0.015}Te$ high-resolution TEM image with an intensity profile inset.

secondary phases, dislocations, strain fields, and Ge vacancy-related planar defects, effectively facilitates full-spectrum phonon scattering. Together with the optimization of electronic transport, these microstructural characteristics synergistically enhance the thermoelectric performance of GeTe-based materials.

Figure 6 illustrates the temperature-dependent thermal properties of the samples GeTe, $Ge_{0.9}Sb_{0.1}Te$, and $Ge_{0.9-x}Sb_{0.1}Ni_xTe$ (x = 0.005–0.02). Progressive doping substantially reduces the κ of GeTe from ~7.7 to ~1.7 $W{\cdot}m^{-1}{\cdot}K^{-1}$ in $Ge_{0.9}Sb_{0.1}Te$ at 323 K, with Ni codoping further lowering this value to ~1.4 $W{\cdot}m^{-1}{\cdot}K^{-1}$ (Fig. 6(a)). To investigate the origin of this reduction, we calculated the κ_e using $\kappa_e = L\sigma T$, where L is the Lorenz constant determined by a two-band model (see the ESM) [63]. The κ_l is then derived from $\kappa = \kappa_e + \kappa_l$. As shown in Fig. 6(b), Sb doping reduces κ_l from ~2.5 $W{\cdot}m^{-1}{\cdot}K^{-1}$ in pristine GeTe to ~1.1 $W{\cdot}m^{-1}{\cdot}K^{-1}$ at 323 K, while Ni codoping further reduces κ_l to ~0.8 $W{\cdot}m^{-1}{\cdot}K^{-1}$. Furthermore, the position where the inflection point appears in thermal conductivity also indicates that doping with Ni and Sb leads to a reduction in the phase transition temperature (Fig. S10 in the ESM). The sound velocity measurements confirmed that Ni doping additionally suppressed phonon propagation beyond the reduction achieved by Sb, contributing to the overall decrease in κ (Fig. 6(c)). This phenomenon is consistent with the mechanism of chemical bond softening reported in Refs. [11,18]. Fundamentally, such an effect arises from multiscale defects generated by Sb and Ni codoping, which effectively impede phonon transport. To quantify the phonon-scattering contributions across different defect scales (Table S4 in the ESM), we employed the Debye–Callaway model [64–66]. The analysis demonstrated that grain boundaries and dislocations serve as primary scattering centers for low-frequency phonons (Fig. 6(d)). Meanwhile, mass/strain fluctuations associated with point defects in conjunction with NiGe nanoprecipitates (10–30 nm) play a major role in suppressing high-frequency phonon propagation. This multiscale phonon scattering, combined with the optimized electrical properties from Ni shallow impurity levels and the reduced thermal conductivity due to NiGe nanoprecipitates, significantly enhanced the thermoelectric performance. This dual mechanism drives synergistic performance enhancement, yielding a peak ZT of 2.15 at 773 K and an average ZT_{avg} of 1.45 across 323–773 K for $Ge_{0.885}Sb_{0.1}Ni_{0.015}Te$ (Fig. 6(e)). We have verified that the TE improvement can be reliably reproduced (Fig. S11 in the ESM). Furthermore, a single-leg device fabricated with Fe electrodes and SnTe bonding layers achieved a conversion

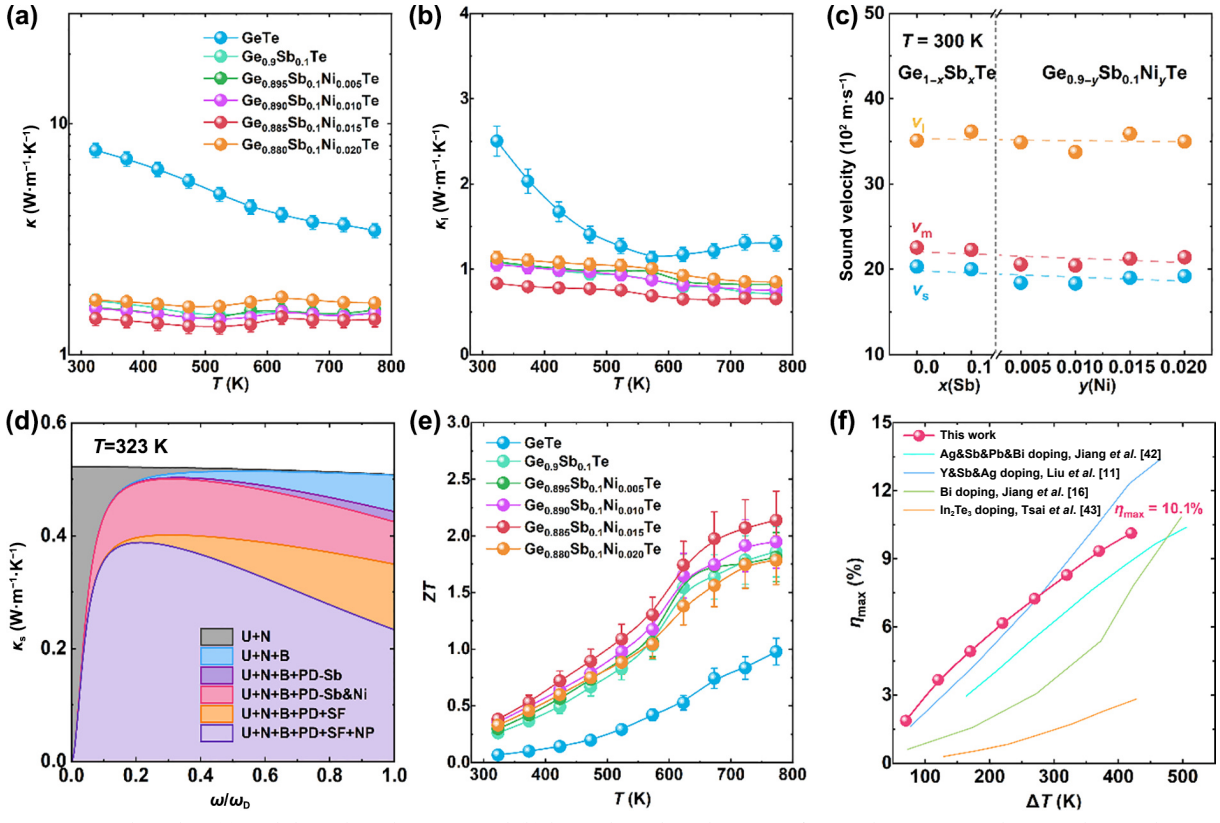

Fig. 6 Temperature-dependent (a) total thermal conductivity κ and (b) lattice thermal conductivity κ_l for samples GeTe, $Ge_{0.9}Sb_{0.1}Te$, and $Ge_{0.9-x}Sb_{0.1}Ni_xTe$ (x = 0.005–0.02). (c) Sound velocity of GeTe-based materials. (d) Debye–Callaway model simulation of phonon scattering contributions in $Ge_{0.885}Sb_{0.1}Ni_{0.015}Te$ at 323 K [64–66]. (e) Temperature-dependent ZT for samples GeTe, $Ge_{0.9}Sb_{0.1}Te$, and $Ge_{0.9-x}Sb_{0.1}Ni_xTe$ (x = 0.005–0.02). (f) Comparison of maximum conversion efficiency η_{max} for a single-leg device using an Fe electrode and SnTe bonding layers with Refs. [11,16,42,43].

efficiency of ~10% at ΔT = 420 K (Figs. S12 and S13 in the ESM). As shown in Fig. 6(f), the performance ranks among the highest reported for analogous systems [11,16,42,43]. The synergistic optimization of shallow impurity engineering and microstructural defect control advances both the performance and application viability of GeTe-based TE materials.

4 Conclusions

In summary, this work demonstrates synergistic optimization of shallow impurity level engineering and multiscale defect engineering through Ni doping in GeTe-based TE. Building upon Sb-doped carrier concentration modulation, Ni introduces shallow impurity levels into GeTe via its unique electronic configuration, promoting valence band convergence and enhancing carrier effective mass. Consequently, $Ge_{0.885}Sb_{0.1}Ni_{0.015}Te$ achieves a Seebeck coefficient of ~232 $\mu V \cdot K^{-1}$ at 773 K. Concurrently, Sb/Ni codoping constructs multiscale defect systems, particularly via *in situ* formation of 10–30 nm NiGe nanophases, which suppress κ_l to ~0.8 $W \cdot m^{-1} \cdot K^{-1}$ at 323 K. Coordinated optimization of electrical and thermal transport yields a peak ZT of 2.15 and an average ZT_{avg} of 1.45 at 773 K for $Ge_{0.885}Sb_{0.1}Ni_{0.015}Te$. A single-leg device fabricated with Fe electrodes and a SnTe interfacial layer attains ~10% conversion efficiency under ΔT = 420 K, representing state-of-the-art performance. This work provides critical support for advancing GeTe-based TE materials toward practical applications.

Acknowledgements

This work was supported by the Guangxi Science and TechnologyProject (No. JF2504850014), the National Natural Science Foundation of China (Nos. U21A2054, 52563035, and 52273285), and the Postdoctoral Science Foundation of China (No. 2024MD763940).

Author contributions

Zhongwei Zhang: writing – review and editing, writing – original draft preparation, formal analysis, conceptualization, data curation. Fengting Mao: methodology, investigation (experimental), validation (characterization). Min Yao: visualization. Shiyuan Zhao: investigation. Sijing Zhu: funding acquisition. Zhengniu Pan: investigation. Jun-Liang Chen: methodology. Zhixiang Zhang: investigation. Qi Zhou: visualization. Wentao Zhang: methodology. Jianmin Chen: methodology. Jie Gao: methodology. Lei Miao: writing – review and editing, writing – original draft preparation, conceptualization, funding acquisition.

Availability of data and materials

The data that support the findings of this study are available from the corresponding author upon reasonable request.

Competing interests

The authors have no competing interests to declare that are relevant to the content of this article.

Electronic Supplementary Material

Supplementary material (Figs. S1–S6, Tables S1–S4, the two Kane bands model and the Debye–Callaway model) is available in the online version of this article at https://doi.org/10.26599/JAC.2026.9221258.

References

[1] Hong M, Li M, Wang Y, *et al.* Advances in versatile GeTe thermoelectrics from materials to devices. *Adv Mater* 2023, **35**: 2208272.

[2] Jiang YL, Yu JC, Li HZ, *et al.* Chemical modulation and defect engineering in high-performance GeTe-based thermoelectrics. *Chem Sci* 2025, **16**: 1617–1651.

[3] Xu SD, Horta S, Lawal A, *et al.* Interfacial bonding enhances thermoelectric cooling in 3D-printed materials. *Science* 2025, **387**: 845–850.

[4] Powell AV, Vaqueiro P, Tippireddy S, *et al.* Exploiting chemical bonding principles to design high-performance thermoelectric materials. *Nat Rev Chem* 2025, **9**: 241–260.

[5] Zhu JJ, Wang Y, Liu H, *et al.* Carbon fiber/thermoelectric Ag_2S core–shell structure-based temperature–pressure dual-mode sensors. *J Adv Ceram* 2025, **14**: 9221073.

[6] Yan X, Pan HJ, Zhang YX, *et al.* Highly enhanced thermoelectric and mechanical performance of copper sulfides via natural mineral *in-situ* phase separation. *J Adv Ceram* 2024, **13**: 641–651.

[7] Li Z, Deng TT, Qiu PF, *et al.* Plasticity of Bi_2Te_3-family thermoelectric crystals. *Nat Commun* 2025, **16**: 5190.

[8] Wen LM, Yin L, Li XF, *et al.* Unified contact layer design for highly efficient segmented PbTe/Bi_2Te_3 thermoelectric devices. *Energ Environ Sci* 2025, **18**: 9939–9948.

[9] Li WP, Yu ZH, Liu CY, *et al.* Superior multiphase interfaces in AgCuTe-based composite with significantly enhanced thermoelectric properties. *J Adv Ceram* 2023, **12**: 1511–1520.

[10] Chang C, Wu MH, He DS, *et al.* 3D charge and 2D phonon transports leading to high out-of-plane *ZT* in n-type SnSe crystals. *Science* 2018, **360**: 778–783.

[11] Liu CY, Zhang ZW, Peng Y, *et al.* Charge transfer engineering to achieve extraordinary power generation in GeTe-based thermoelectric materials. *Sci Adv* 2023, **9**: eadh0713.

[12] Jiang YH, Wei TR, Shi X. Beyond phase-change materials: Pseudo-binary $(GeTe)_n(Sb_2Te_3)_m$ alloys as promising thermoelectric materials. *Mater Today Phys* 2023, **36**: 101167.

[13] Jin Y, Ren DD, Qiu YT, *et al.* Electrical and thermal transport properties of $Ge_{1-x}Pb_xCu_ySb_yTeSe_{2y}$. *Adv Funct Mater* 2023, **33**: 2304512.

[14] Zhang CH, Yan G, Wang YB, *et al.* Grain boundary complexions enable a simultaneous optimization of electron and phonon transport leading to high-performance GeTe thermoelectric devices. *Adv Energy Mater* 2023, **13**: 2203361.

[15] Kimber SAJ, Zhang JY, Liang CH, *et al.* Dynamic crystallography reveals spontaneous anisotropy in cubic GeTe. *Nat Mater* 2023, **22**: 311–315.

[16] Jiang YL, Dong JF, Zhuang HL, *et al.* Evolution of defect structures leading to high *ZT* in GeTe-based thermoelectric materials. *Nat Commun* 2022, **13**: 6087.

[17] Bu ZL, Zhang XY, Shan B, *et al.* Realizing a 14% single-leg thermoelectric efficiency in GeTe alloys. *Sci Adv* 2021, **7**: eabf2738.

[18] Sarkar D, Das S, Taneja V, *et al.* Glassy thermal transport triggers ultra-high thermoelectric performance in GeTe. *Adv Mater* 2025, **37**: 2417561.

[19] Waghmare UV, Spaldin NA, Kandpal HC, *et al.* First-principles indicators of metallicity and cation off-centricity in the IV–VI rocksalt chalcogenides of divalent Ge, Sn, and Pb. *Phys Rev B* 2003, **67**: 125111.

[20] Sun Q, Li M, Shi XL, *et al.* Versatile vanadium doping induces high thermoelectric performance in GeTe via band alignment and structural modulation. *Adv Energy Mater* 2021, **11**: 2100544.

[21] Feng YM, Li JQ, Li Y, *et al.* Band convergence and carrier-density fine-tuning as the electronic origin of high-average thermoelectric performance in Pb-doped GeTe-based alloys. *J Mater Chem A* 2020, **8**: 11370–11380.

[22] Liang RN, Yan G, Geng Y, *et al.* Compromise design of resonant levels in GeTe-based alloys with enhanced thermoelectric performance. *Adv Funct Mater* 2024, **34**: 2404021.

[23] Guo Z, Wu G, Tan XJ, *et al.* Enhanced thermoelectric performance in GeTe by synergy of midgap state and band convergence. *Adv Funct Mater* 2023, **33**: 2212421.

[24] Hu MH, Li M, Wang DZ, *et al.* Revisiting cobalt dopability in GeTe system to design modulation-doped thermoelectrics. *Adv Funct Mater* 2025, **35**: 2421837.

[25] Hong M, Wang Y, Feng TL, *et al.* Strong phonon–phonon interactions securing extraordinary thermoelectric $Ge_{1-x}Sb_xTe$ with Zn-alloying-induced band alignment. *J Am Chem Soc* 2019, **141**: 1742–1748.

[26] Hong M, Wang Y, Liu WD, *et al.* Arrays of planar vacancies in superior thermoelectric $Ge_{1-x-y}Cd_xBi_yTe$ with band convergence. *Adv Energy Mater* 2018, **8**: 1801837.

[27] Wu LH, Li X, Wang SY, *et al.* Resonant level-induced high thermoelectric response in indium-doped GeTe. *NPG Asia Mater* 2017, **9**: e343.

[28] Hong M, Chen ZG, Yang L, *et al.* Realizing *zT* of 2.3 in $Ge_{1-x-y}Sb_xIn_yTe$ via reducing the phase-transition temperature and introducing resonant energy doping. *Adv Mater* 2018, **30**: 1705942.

[29] Luo ZZ, Cai ST, Hao SQ, *et al.* High figure of merit in gallium-doped nanostructured n-type PbTe–*x*GeTe with midgap states. *J Am Chem Soc* 2019, **141**: 16169–16177.

[30] Li J, Hu Q, He S, *et al.* Enhancing near-room-temperature GeTe thermoelectrics through In/Pb co-doping. *ACS Appl Mater Inter* 2021, **13**: 37273–37279.

[31] Srinivasan B, Gellé A, Gucci F, *et al.* Realizing a stable high thermoelectric $zT \sim 2$ over a broad temperature range in $Ge_{1-x-y}Ga_xSb_yTe$ via band engineering and hybrid flash-SPS processing. *Inorg Chem Front* 2019, **6**: 63–73.

[32] Zhong JX, Yang XY, Lyu T, *et al.* Nuanced dilute doping strategy enables high-performance GeTe thermoelectrics. *Sci Bull* 2024, **69**: 1037–1049.

[33] Chen YQ, Li M, Wang XD, *et al.* Copper ion diffusion by solid solution treatment advancing GeTe-based thermoelectrics. *Nat Commun* 2025, **16**: 6796.

[34] Chen QY, Yang C, Xing T, *et al.* Defect engineering and alloying strategies for tailoring thermoelectric behavior in GeTe and its alloys. *J Materiomics* 2025, **11**: 100832.

[35] Zhu JL, Li RH, Tan XB, *et al.* Synergistic optimization of electronic and thermal properties in single-stage GeTe thermoelectric devices. *J Am Chem Soc* 2025, **147**: 37555–37564.

[36] Cheng JH, Lyu T, Liang GG, *et al.* Microstructure design via novel thermodynamic route to enhance the thermoelectric performance of GeTe. *Mater Today Phys* 2022, **27**: 100820.

[37] Parashchuk T, Wiendlocha B, Cherniushok O, *et al.* Multiple defect states engineering towards high thermoelectric performance in GeTe-based materials. *Chem Eng J* 2024, **499**: 156250.

[38] Yu Y, Xie L, Pennycook SJ, *et al.* Strain-induced van der Waals gaps in GeTe revealed by *in situ* nanobeam diffraction. *Sci Adv* 2022, **8**: eadd7690.

[39] Mao FT, Zhang ZW, Zhu SJ, *et al.* A core–shell structure to realize high thermoelectric performance in Fe and Sb co-doped GeTe materials. *J Materiomics* 2026, **12**: 101108.

[40] Zheng Z, Su XL, Deng RG, *et al.* Rhombohedral to cubic conversion of GeTe via MnTe alloying leads to ultralow thermal conductivity, electronic band convergence, and high thermoelectric performance. *J Am Chem Soc* 2018, **140**: 2673–2686.

[41] Li X, Liu M, Guo MC, *et al.* Tailoring band structure and Ge precipitates through Er and Sb/Bi co-doping to realize high thermoelectric performance in GeTe. *Chem Eng J* 2023, **474**: 145820.

[42] Jiang BB, Wang W, Liu SX, *et al.* High figure-of-merit and power generation in high-entropy GeTe-based thermoelectrics. *Science* 2022, **377**: 208–213.

[43] Tsai YF, Yang MJ, Deng JR, *et al.* Reducing domain density enhances conversion efficiency in GeTe. *Small* 2024, **20**: 2312206.

[44] Zhi SZ, Li JB, Hu LP, *et al.* Medium entropy-enabled high performance cubic GeTe thermoelectrics. *Adv Sci* 2021, **8**: 2100220.
[45] Tabatabaei K, Sully HR, Ju Z, *et al.* Structural insights on microwave-synthesized antimony-doped germanium nanocrystals. *ACS Nano* 2021, **15**: 1685–1700.
[46] Chen S, Bai H, Wu H, *et al.* The role of Ge vacancies and Sb doping in GeTe: A comparative study of thermoelectric transport properties in $Sb_xGe_{1-1.5x}Te$ and $Sb_xGe_{1-x}Te$ compounds. *Mater Today Phys* 2022, **24**: 100682.
[47] He J, Tritt TM. Advances in thermoelectric materials research: Looking back and moving forward. *Science* 2017, **357**: eaak9997.
[48] Zhang XY, Bu ZL, Lin SQ, *et al.* GeTe thermoelectrics. *Joule* 2020, **4**: 986–1003.
[49] Xie CH, Fan YT, Liu ZY, *et al.* Enhancing thermoelectric efficiency in GeTe via tailored alloying and band engineering. *Chem Mater* 2025, **37**: 4917–4924.
[50] Liu M, Guo MC, Yang YX, *et al.* Tailoring the electron and phonon transport in metavalently bonded GeTe by stepwise doping. *Adv Energy Mater* 2025, **15**: 2405178.
[51] Wang TT, Guo QS, Feng JH, *et al.* Screening of promising thermoelectric materials from MnTe–GeTe alloying. *Mater Today Phys* 2025, **51**: 101661.
[52] Liu SX, Wang W, Xie L, *et al.* Realizing high thermoelectric performance in GeTe-based alloys without lead addition. *Adv Funct Mater* 2026, **36**: e10362.
[53] Sun H, Lu X, Chi H, *et al.* Highly efficient $(In_2Te_3)_x(GeTe)_{3-3x}$ thermoelectric materials: A substitute for TAGS. *Phys Chem Chem Phys* 2014, **16**: 15570–15575.
[54] Garmroudi F, Di Cataldo S, Parzer M, *et al.* Energy filtering–induced ultrahigh thermoelectric power factors in Ni_3Ge. *Sci Adv* 2025, **11**: eadv7113.
[55] Zhang W, Ronneberger I, Li Y, *et al.* Magnetic properties of crystalline and amorphous phase-change materials doped with 3*d* impurities. *Adv Mater* 2012, **24**: 4387–4391.
[56] Liu WD, Wang DZ, Liu QF, *et al.* High-performance GeTe-based thermoelectrics: From materials to devices. *Adv Energy Mater* 2020, **10**: 2000367.
[57] Hong M, Chen ZG. Chemistry in advancing thermoelectric GeTe materials. *Acc Chem Res* 2022, **55**: 3178–3190.
[58] Li HQ, Chen C, Cheng JX, *et al.* Lead-free GeTe alloys with high thermoelectric performance for low-grade waste heat energy harvesting. *Nano Energy* 2025, **136**: 110690.
[59] Sun QQ, Chen KY, Tan XJ, *et al.* Microstructure manipulation achieves superior efficiency of GeTe-based thermoelectric modules. *Small* 2025, **21**: 2500333.
[60] Xiang S, Zhang Y, Song M, *et al.* Observation of the impact of dislocations on atomic polarization and domain structures in $BaTiO_3$. *Adv Phys Res* 2025, **4**: 2500042.
[61] Zhuo FP, Wang B, Cheng L, *et al.* Unlocking electrostrain in plastically deformed barium titanate. *Adv Mater* 2024, **36**: 2413713.
[62] Yu Y, Xu X, Wang Y, *et al.* Tunable quantum gaps to decouple carrier and phonon transport leading to high-performance thermoelectrics. *Nat Commun* 2022, **13**: 5612.
[63] Li J, Zhang XY, Lin SQ, *et al.* Realizing the high thermoelectric performance of GeTe by Sb-doping and Se-alloying. *Chem Mater* 2017, **29**: 605–611.
[64] Debye PP, Conwell EM. Electrical properties of N-type germanium. *Phys Rev* 1954, **93**: 693–706.
[65] Callaway J, von Baeyer HC. Effect of point imperfections on lattice thermal conductivity. *Phys Rev* 1960, **120**: 1149–1154.
[66] Hu CL, Xia KY, Fu CG, *et al.* Carrier grain boundary scattering in thermoelectric materials. *Energ Environ Sci* 2022, **15**: 1406–1422.